Princeton Plasma Physics Laboratory

PPPL- 4821

PPPL- 4821

Dynamics of the Disruption Halo Current Toroidal Asymmetry in NSTX

S.P. Gerhardt

September, 2012

PPPL PRINCETON PLASMA PHYSICS LABORATORY

Prepared for the U.S. Department of Energy under Contract DE-AC02-09CH11466.

Princeton Plasma Physics Laboratory
Report Disclaimers

Full Legal Disclaimer

Trademark Disclaimer

PPPL Report Availability

Princeton Plasma Physics Laboratory:

http://www.pppl.gov/techreports.cfm

Office of Scientific and Technical Information (OSTI):

http://www.osti.gov/bridge

Related Links:

U.S. Department of Energy

Office of Scientific and Technical Information

Fusion Links

Dynamics of the Disruption Halo Current Toroidal Asymmetry in NSTX

S.P. Gerhardt[1]

1: Princeton Plasma Physics Laboratory, Princeton, New Jersey, USA, 08543

Abstract

This paper describes the dynamics of disruption halo current non-axisymmetries in the lower divertor of the National Spherical Torus Experiment [M. Ono, et al. Nuclear Fusion 40, 557 (2000)]. While. The halo currents typically have a strongly asymmetric structure where they enter the divertor floor, and this asymmetry has been observed to complete up to 7 toroidal revolutions over the duration of the halo current pulse. However, the rotation speed and toroidal extend of the asymmetry can vary significantly during the pulse. The rotation speed, halo current pulse duration, and total number of revolutions tend to be smaller in cases with large halo currents. The halo current pattern is observed to become toroidally symmetric at the end of the halo current pulse. It is proposed that this symmeterization is due to the loss of most or all of the closed field line geometry in the final phase of the vertical displacement event.

Keywords: Disruption, NSTX, Spherical Torus, Halo Currents
PACS numbers: 52.55.Fa

Contents:
7 Sections
14 Figures
70 References

Sections:

1: Introduction

Tokamak plasmas are prone to events known as disruptions [1,2] where an extremely rapid breakdown of plasma confinement, known at the thermal quench [1,2] leads to a sudden decay of the plasma current in the then cold plasma [3-8]; this latter phase is called the current quench. The thermal loading during the thermal quench [1,2,9-13] can lead to severe melting or ablation of the plasma facing components, while the eddy currents driven by the current quench can lead to large forces on in-vessel structures [11]. Finally, it is possible for a large fraction of the plasma current to be converted to a runaway electron beam [1,2,14-23], potentially leading to severe localized damage to in-vessel components if position control of the beam is not maintained [24].

Beyond these three effects, there is a fourth damaging phenomenon during a disruption. The control of the plasma vertical position is often lost during a disruption, resulting in a "Vertical Displacement Event", or VDE. The VDE results in the plasma coming in contact with the plasma facing components (PFCs) at the top or bottom of the confinement chamber. Currents have been observed to flow from the plasma into the PFCs, through the various in-vessel structures, and then out of a different set of PFCs back into the plasma. These currents, which have historically been known as "halo currents", have been observed in the conventional aspect ratio tokamaks DIII-D [3,25-28], JET [29-34], ASDEX-Upgrade [35,36], COMPASS-D [37], JT-60 [38] and ALCATOR C-MOD [39], and in the spherical torii MAST [40] and NSTX [41]. When the current path in these in-vessel components crosses the strong tokamak magnetic field, the resulting JxB forces can result in severe damage.

The dynamics of these halo currents can be quite complex. For instance, they need not be axisymmetric; toroidal peaking factors of these currents, defined as the maximum detected halo current normalized by the mean halo current for a toroidal distributed array of sensors, have been observed with values exceeding 4 in conventional aspect ratio tokamaks [2]. Hence, the forces can be concentrated on a subset of the tokamak components. Furthermore, the halo current asymmetries have been observed to rotate toroidally [34,39]. If the rotation frequencies are a match to the resonant frequencies of the various in-vessel components, then the potential for damage is further increased [34]. As a consequence of their damaging potential, the details of these non-axisymmetric halo currents have been the subject of numerous recent theoretical studies [42-46], largely developing the idea that the non-axisymmetric halo currents are surface currents that develop to stabilize the otherwise Alfvenic growth of the external kink mode.

This paper expands on the NSTX halo current data presented in Ref. [41], by focusing on spatial and temporal dynamics of the currents where they enter the divertor floor. Section 2 describes the NSTX device and halo current measurements. Section 3 describes the observations of halo current rotation, using examples from a number of discharges. Section 4 examines some statistics of the halo current rotation, while section 5 examines the impact of large n=1 applied fields on the rotational dynamics. Section 6

proposes an explanation for the observe halo current symmeterization late in the halo current pulse. A summary and discussion are provided in section 7.

Finally, it is worth noting that various terminology has been used recently for these currents. Historically, they have been referred to as "halo currents", or possible "disruption halo currents". Recent work by Zakharov [43] has introduced the phrases "Evans Currents" and "Hiro Currents", denoting different mechanisms that can drive these currents. From a purely experimental perspective, it appears that a phrase such as "disruption scrape-off layer currents" would be most accurate. However, in this paper, the phrase "halo currents" will be used in order to be consistent with previous experimental usage, and without any judgment about the underlying physics.

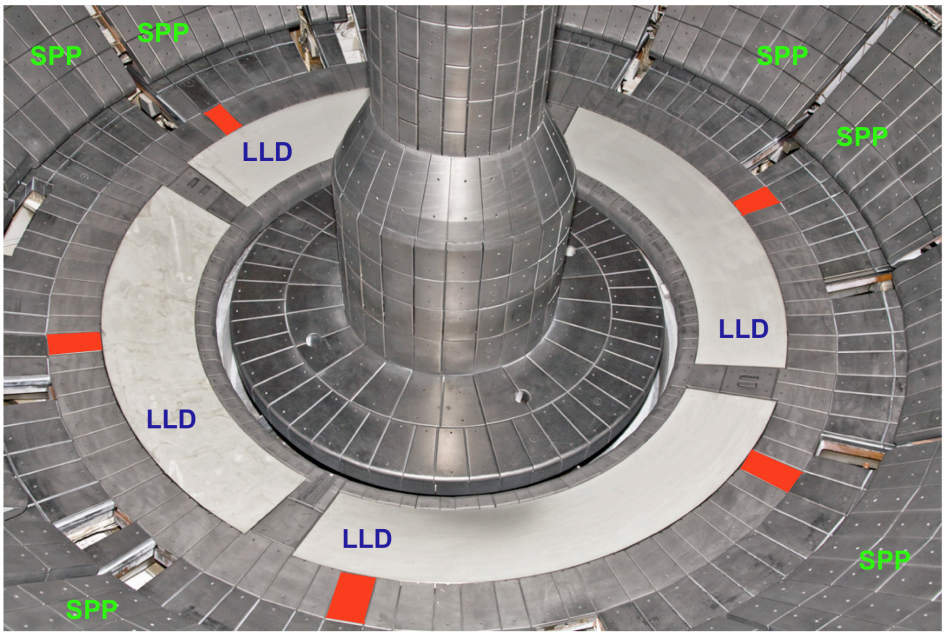

Fig 1: Location (in red) of the row-3 shunt tile diagnostics used for the measurements in this paper. A sixth tile is located behind the center column. For reference, both the liquid lithium divertor (LLD) and secondary passive plates (SPPs) are labeled.

2: NSTX Device and Halo Current Instrumentation.

NSTX [47] is a medium scale spherical torus located at Princeton Plasma Physics Laboratory. The typical major radius of the plasma is 0.85 meters, with aspect ratios of $1.35<A<1.55$. Typical plasma currents are in the range $500 < I_P$ [kA] < 1300, with toroidal fields in the range $0.35 < B_T$ [T] < 0.55. Neutral beam heating [48] powers are typically up to 7 MW, with high-harmonic fast wave (HHFW) power [49] up ~6 MW at 30 MHz.

As described in Ref. [50], NSTX has been outfitted with a diverse array of halo current diagnostics. The data from these various diagnostics was described in great detail in Ref. [41]. This paper focuses on a detailed analysis of a small subset of that data, namely, the data collected by the lower outer divertor "shunt tiles".

The locations of these tiles are indicated in the photograph in Fig. 1; also indicated in the figure are the liquid lithium divertor [51] trays, and the secondary passive plates. These shunt tiles are fitted with compact resistive shunts where they are fastened to the divertor floor; the voltage on these shunts is used to infer the current flowing into the tile. This shunt tile data was digitized at both 5 kHz and 500 kHz. Only the faster sampled data is used in this paper. The local current densities are calculated as the current collected by each tile normalized by the area of the face of each tile. Furthermore, the set of shunt tiles in Fig. 1 was only available during the 2010 run campaign. Hence, all data illustrated in this paper come from that run period.

For reference, the plasma current direction was counter-clockwise when viewed from above, or into the plane of figures 2b) and 5b). The toroidal field (TF) rod current was downward, leading to a toroidal field in the clockwise direction when viewed from above. The NSTX neutral beams, used in all discharges described in detail in sections 3, 5, & 6 and most in the database analysis in Section 4, are oriented in the co-injection direction, i.e. injection parallel to the plasma current.

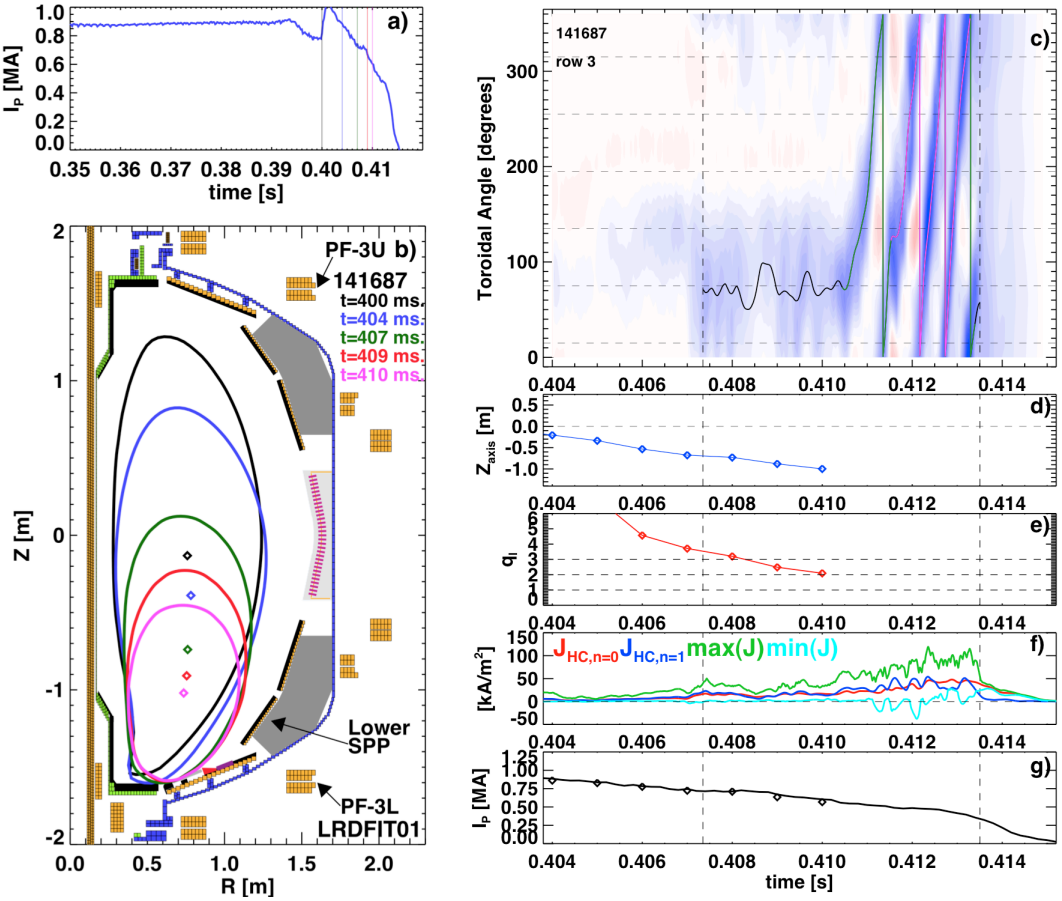

Fig 2: Dynamics of a discharge that shows significant halo current rotation. Shown are a) the plasma current and b) plasma motion leading up to the large halo current phase, c) the contours of halo currents in the lower divertor row #3 vs. time and toroidal angle, d) the magnetic axis position, e) the edge safety factor, and f) the n=0 & n=1 components of the halo current, as well as the maximum and minimum values of the halo current on any single tile, and g) the plasma current again.

3: Observation of halo current rotation in the NSTX divertor

As stated in the introduction, there have been numerous instances where many toroidal revolutions of the halo current pattern occur during the disruption. An example of this discharge variety is in Fig. 2. Fig 2a) shows the plasma current evolution and Fig. 2b) shows the reconstruct plasma boundary for time slices immediately before the phase with large halo currents. The colors of the boundary reconstructions correspond to the times of the vertical lines in the plasma current trace. It is clear that this case is a downward VDE, with the point of contact on the inner half of the lower outer divertor.

The contours of the halo current pattern as a function of toroidal angle and time are shown in Fig. 2c); the colors are arbitrarily scaled so that the darkest blue corresponds to the maximum current out of the tiles for this particular case. Some small amount of current begins to flow just after t=0.407 s. This current is largely localized to three adjacent tiles (from a total of six) and flows for ~3 ms at this toroidal angle. Throughout this phase of small halo current, the edge safety factor (q_l) is constantly decreasing as the plasma moves down and the cross-section shrinks at approximately constant I_P. As q_l decreases to 2 at about t=0.41 s in Fig. 2e), two significant changes in the nature of the currents can be observed. First, there is a gradual increase in the halo current magnitude. Second, the non-axisymmetric component of the halo current pattern begins to rotate. In this particular case, approximately four complete circuits of the divertor are made by the asymmetry. The direction of rotation is opposite that of the plasma current, and opposite to that induced by the co-injected neutral beams.

This rotation is emphasized in Fig. 2c) by the black, green, and magenta lines tracing out the contours; these curves are determined as follows. At each time slice, the toroidal variation of the halo current is fit to a form:

$$J_{HC}(\phi) = J_{HC,n=0} + J_{HC,n=1}\cos(\phi - \phi_{n=1}) \quad (1)$$

Here, $J_{HC,n=0}$, $J_{HC,n=1}$, and $\phi_{n=1}$ are fit parameters. Of course, the actual toroidal distribution may be significantly more peaked than a simple cosine; this fit is simply used to track the phase and approximate asymmetry magnitude. More complex fits, which allow the toroidal extent of the halo current to be properly tracked, will be discussed later in this section. The black, green, and magenta contour in Fig. 2c) is then the time dependent phase $\phi_{n=1}$ determined by this fitting procedure for Eqn. 1.

The colors are indicative of various times in the halo current pulse, as indicated schematically by Fig. 3a. The n=1 component of a *model* halo current pulse is shown in that figure. The duration where the current is greater than 75% of the maximum is indicated in magenta, greater than 50% in green, and greater than 25% in black. These various time windows are well defined for any given pulse shape. In the analysis below, quantities will be averaged over these windows.

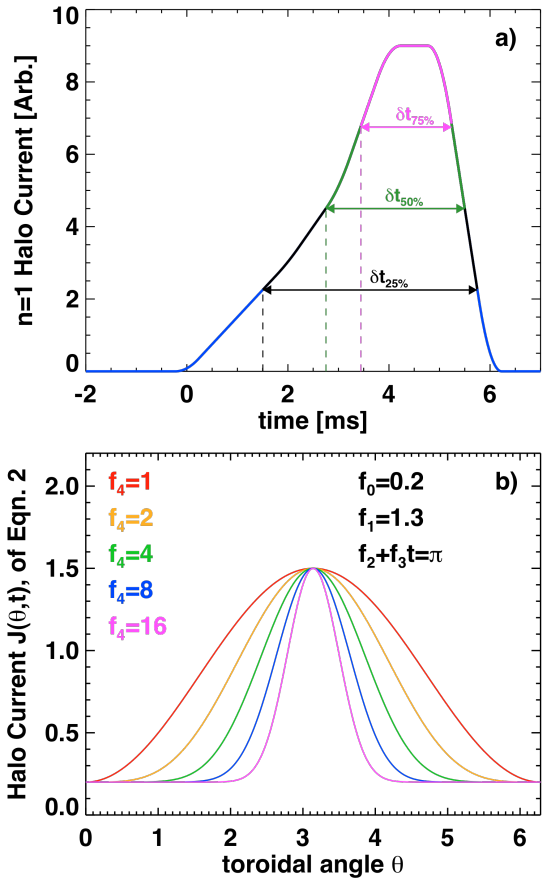

Fig. 3: a) Definition of the 25%, 50%, and 75% levels for halo current pulse analysis, and b) model curves showing the toroidal dependence of the fitting function Eqn 2. See text for further details.

Fig. 2f) & 2g) show additional details of the halo & plasma current evolution. The n=0 and n=1 components of the halo current, determined from fits to eqn. 1, are indicated in red and blue respectively. These components have similar magnitude through the majority of the pulse. This observation, along with the contours in Fig. 2c), indicate that the fundamental structure of the current entering the divertor floor is a toroidally localized lobe. The approximately equal n=0 and n=1 components are present because, at any given poloidal location, the halo currents tend to have only a single sign; it is rare for current to both flow into some tiles and out of others at the same poloidal location.

This last statement is made clear by the traces of the minimum and maximum halo current flowing in any of the 6 tiles, also shown in Fig. 2f. The maximum value tends to be approximately equal to the sum of the n=1 and n=1 parts, while, except for brief transients, the minimum value hovers around zero. Note that the similar contour plot from AUG, Fig. 15 of Ref [36], shows a similar large lobe structure.

The primary exception to the observation of strong asymmetries can be found after t=0.4135 in the Figs 2c) and 2f). After this time, the non-axisymmetric component

of the halo current decays rapidly, leaving behind a largely axisymmetric residual current; the values of min(J), max(J), and $J_{HC,n=0}$ overlap during this phase. This residual n=0 current decays at a rate comparable to the plasma current. As will be shown in Sect. 6, it appears that this corresponds to the phase when the magnetic axis has been nearly or completely driven into the divertor floor, and open field line currents dominate.

More details of the halo current asymmetry dynamics for this discharge can be observed in Fig. 4. In this figure, a more sophisticated fitting function for the toroidal dependence is used, given by Eqn. (2):

$$J(\phi,t) = f_0 + f_1 \frac{\left(1+\cos\left(\phi - f_2 - f_3 t\right)\right)^{f_4}}{2^{f_4}}. \qquad (2)$$

Examples curves of this function are shown in Fig. 3b). f_0 represents the toroidally uniform current amplitude, while f_1 represents the amplitude of any toroidal peaking. The parameter f_3 is the rotation frequency, that, along with offset phase f_2, determine the instantaneous toroidal phase of the asymmetry; the example curves in Fig. 3b) have $f_2+f_3t=\pi$, in order to center the waveform in the plot window. The parameter f_4 controls the width of the peak in toroidal angle. This parameter is scanned from 1 to 16 in the example in Fig. 3b), showing how this fit function can represent toroidally localized halo currents.

To apply this fit, the data is broken into small time windows of duration δt, and the $6\delta t/\tau_s$ data points in each window are used to constrain the fit; here, the 6 refers to the number of shunt tiles and τ_s is the sampling interval. A non-linear fitting routine (lmfit, from Ref [Markwardt 2008]) is then used to fit the parameters during this time window; note that it is only by fitting within a time window long enough for some halo current rotation to occur that the parameter f_3 can be determined. Hence, each of the parameters f_0 through f_4 determined by the fits corresponds to the average value over the small time windows. δt of 0.1 ms has been used for the calculations in this paper.

Four features of this fit function and fitting method are worth noting. First, if a fit function does not include some time dependence, but rather only toroidal angle dependence, then it can less accurately model highly peaked functions, which may only instantaneously manifest themselves on a single tile. However, if the feature is rotating, then the motion of the features across the tiles can be captured in the time dependence of eqn. 2. Of course, if the feature is both toroidally peaked and nearly stationary, then it can be difficult assess even with Eqn 2. Secondly, the toroidal rotation velocity is a direct parameter in the fit, allowing it to be calculated without the noise-inducing differentiation of the asymmetry phase ($\phi_{n=1}$) vs. time. Third, the fit function only works well when there is a single toroidal lobe; less common cases with n=2 (or higher) variation cannot be fit. Finally, it should be noted that an alternative means of writing the function in Eqn. 2 is $J(\phi,t) = f_0 + f_1 \cos^{2f_4}\left(\frac{\phi - f_2 - f_3 t}{2}\right)$.

The results of such a fit are shown in Fig. 4, for the same discharge (141687) as in Fig. 2. Fig. 4a) shows the parameters f_0 and f_1 as black dashed and solid lines respectively. A related version of the parameter f_1, derived from fitting the toroidal dependence at each individual time-slice using a version of Eqn. 2) with no parameter f_3, is shown with a red dashed line. A comparison of these two values of f_1 shows that fitting during windows with an explicit time dependence (solid black) produces a more smooth amplitude than fitting at each time point individually (red dashed). The non-axisymmetric part of the current (f_1) is completely dominant, with the parameter f_0 oscillating around zero for most of the discharge. It is only at the end of the halo current pulse, during the symmeterization phase, that the parameter f_0 becomes large compared to f_1.

The green trace in Fig. 4a) shows the maximum current detected on any single shunt tile at each time, while the cyan trace shows the minimum current on any tile. This metric is motivated by the observation that for f_0=0, the parameter f_1 is exactly equal to the maximum current. As expected, the green trace overlaps the value of f_1, except for during those brief periods where f_0 and the minimum local current are non-zero.

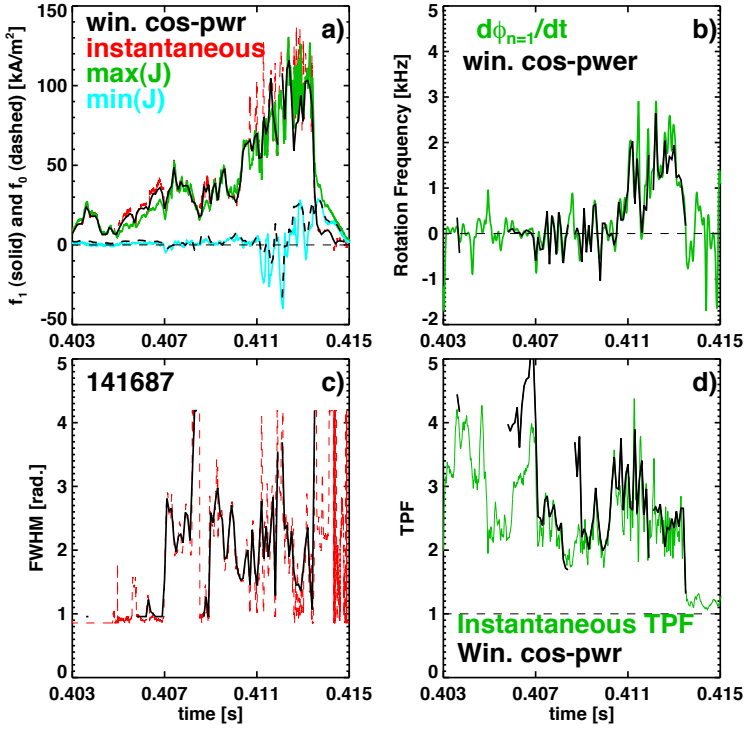

Fig. 4: Details of the toroidal asymmetry evolution for the discharge in Fig. 2. Shown are a) the axisymmetric and non-axisymmetric amplitude components, as well as the maximum and minimum current on any individual tile, b) the toroidal rotation frequency of the perturbation determined by two different methods, and the c) full width at half maximum and d) toroidal peaking factor of the halo currents. The red curves in a) and c) come from fits of eqn.2 at each time slide individually, with the f_3 term eliminated. The phrase "win. cos-pwr" refers to the windowed cosine-power fits of eqn. 2. See text for further details.

The average velocity of the perturbation is shown in Fig. 4b). The velocity $f_3/2\pi$, as determined by the fits of Eqn. 2 within the time windows, is shown in black. The velocity in green results from differentiating the time dependent toroidal phase $\phi_{n=1}$ from

the fits of Eqn. 1. Good agreement is found between the two methods. During the phase 0.406<t<0.410, both calculations show the velocity oscillating about 0 kHz. Starting at t=0.410, the asymmetry begins to rotate, with speeds of typically 1.5-2.0 kHz. However, there is a brief pause in the rotation in this phase of high rotation at t=0.4115 s, visible somewhat subtly in Fig. 2c) and clearly in Fig. 4b).

Figs. 4c) and 4d) show additional dynamics of the toroidal asymmetry. The full-width at half maximum of the fit toroidal distribution is shown in Fig. 4c). Values from both the windowed time-dependent fits (black) and the instantaneous fits (red dashed) are shown, and the benefits of using the full Eqn. 2) with an explicit frequency term in reducing variations in the fit parameters are clear. Early in the halo current pulse, the toroidal width is typically ~2 radians. During the high rotation phase starting at t=0.41, the width varies from ~1.5 radians up to 3 radians, and then back toward 1.4 radians again. The toroidal peaking factor in Fig. 4d) is calculated both using the raw data at each time slice (blue), and using the fit Eqn 2). The two methods generally agree well, and shown significant variation in time.

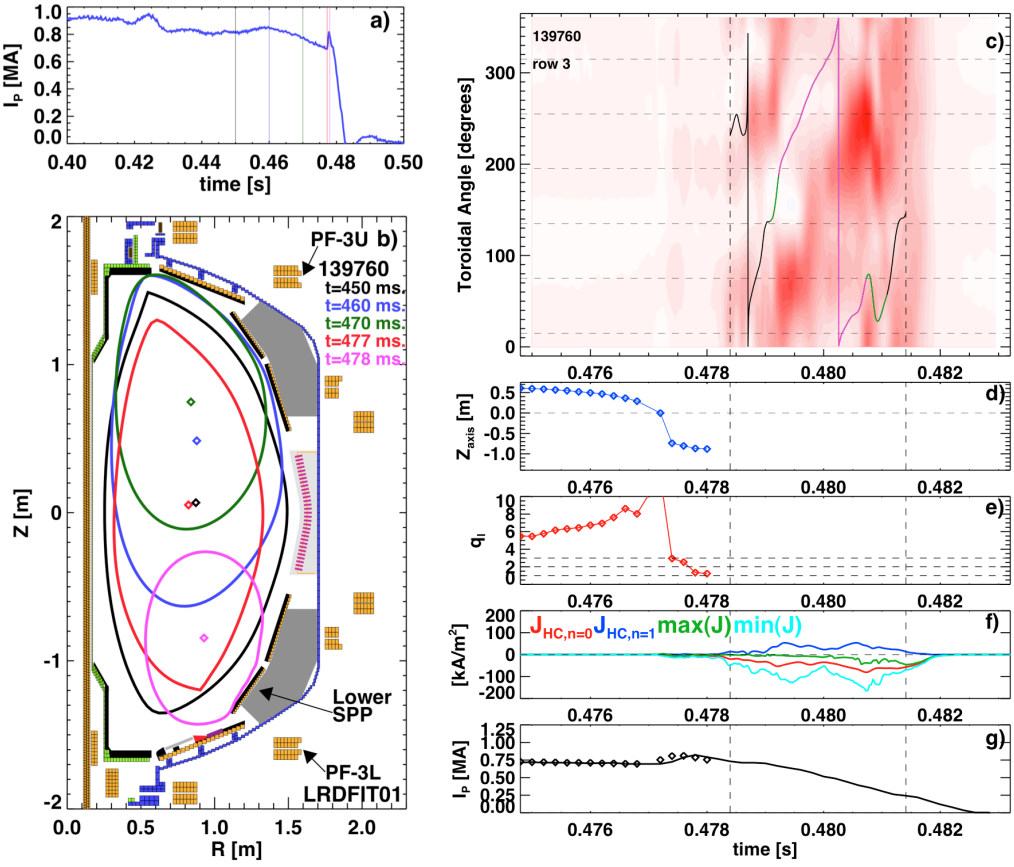

Fig 5: Example of halo current dynamics for a case where the plasma limits on the lower secondary passive plates (SPP). The individual frames show the same quantities as in Fig. 2. Frame c) shows that ~1.75 revolutions of the halo current asymmetry occur in this case.

As described in detail in Ref. [41], VDEs with the trajectory in Fig. 2, where the plasma lands on the outboard divertor floor, are the most common in NSTX. However, it is also reasonably common to find examples where the VDE lands on the secondary passive plates (SPPs). While most of the halo field lines strike the passive plates in these examples, some also land on the outboard divertor, where halo currents are measured. An example of such a case is shown in Fig. 5.

Fig. 5a) shows that the initially centered plasma first drifts upward following a β collapse at t=0.42. The vertical position control system attempts to counteract this motion, and in doing so actively drives the plasma into the lower secondary passive plate. The vertical motion leading up to the final disruption is shown in Fig. 5d), when it is clear that the plasma move very rapidly downward at t~0.477 s. Interestingly, the edge safety factor in Fig 5e) actually increases for a phase, as the plasma cross section increase as it moves off the upper divertor. However, the edge q then drops rapidly when the plasma strikes the lower secondary passive plates.

The contours of halo current density are shown in Fig. 5c. Once again, it is clear that there is i) significant toroidal asymmetry in the outboard divertor halo current pattern, and ii) significant rotation of the asymmetry, again in the direction opposite the plasma current. In this case, the pattern completes almost two toroidal transits during the halo current pulse. However, the magnitude is far more irregular in time compared to the example in Fig. 2, potentially due to the location of these sensors farther from the VDE limiting point.

Fig. 5f) shows that the n=1 and n=0 components of the halo current again have comparable magnitude; the signs are different in this case, since the current is, on average, flowing into the divertor floor in this case, instead of out as in Fig. 2. In this case, the maximum halo current hovers around zero, while the minimum current is in magnitude comparable the sums of the n=0 and 1 parts. This reinforces the observation of the dominant structure being a toroidally localized lobe. Also as before, the halo current asymmetry decays at the end of the pulse, leaving a brief period of dominant n=0 halo current. This discharge will be discussed again in Sect. 6.

Finally, Fig. 6 shows four additional examples of these dynamics for disruptions that limit on the outboard divertor floor, as in Fig. 2. In each case, the halo current contours are shown in the large frame, with the n=0 & 1 decompositions, the minimum and maximum currents at any individual tile, and the plasma current waveforms in the lower frames. The Figs. a) through f) illustrate examples with large currents, but minimal rotation; these two discharges have the largest halo current magnitudes observed by the row-3 shunt tiles in NSTX during the 2010 run campaign. Note that there is almost no discernable toroidal rotation in a), and less than a full revolution in frame d) during the phase of large halo currents. Also note that the contours in Fig 6a) cannot always be described with a single lobe. For instance, at t=0.45 s, current is observed in the tiles at 15 and 75 degrees, as well as at 195 degrees, but with little current on the tiles between. Hence, the fits using Eqn. 2 would not produce meaningful results for this phase of the halo current pulse.

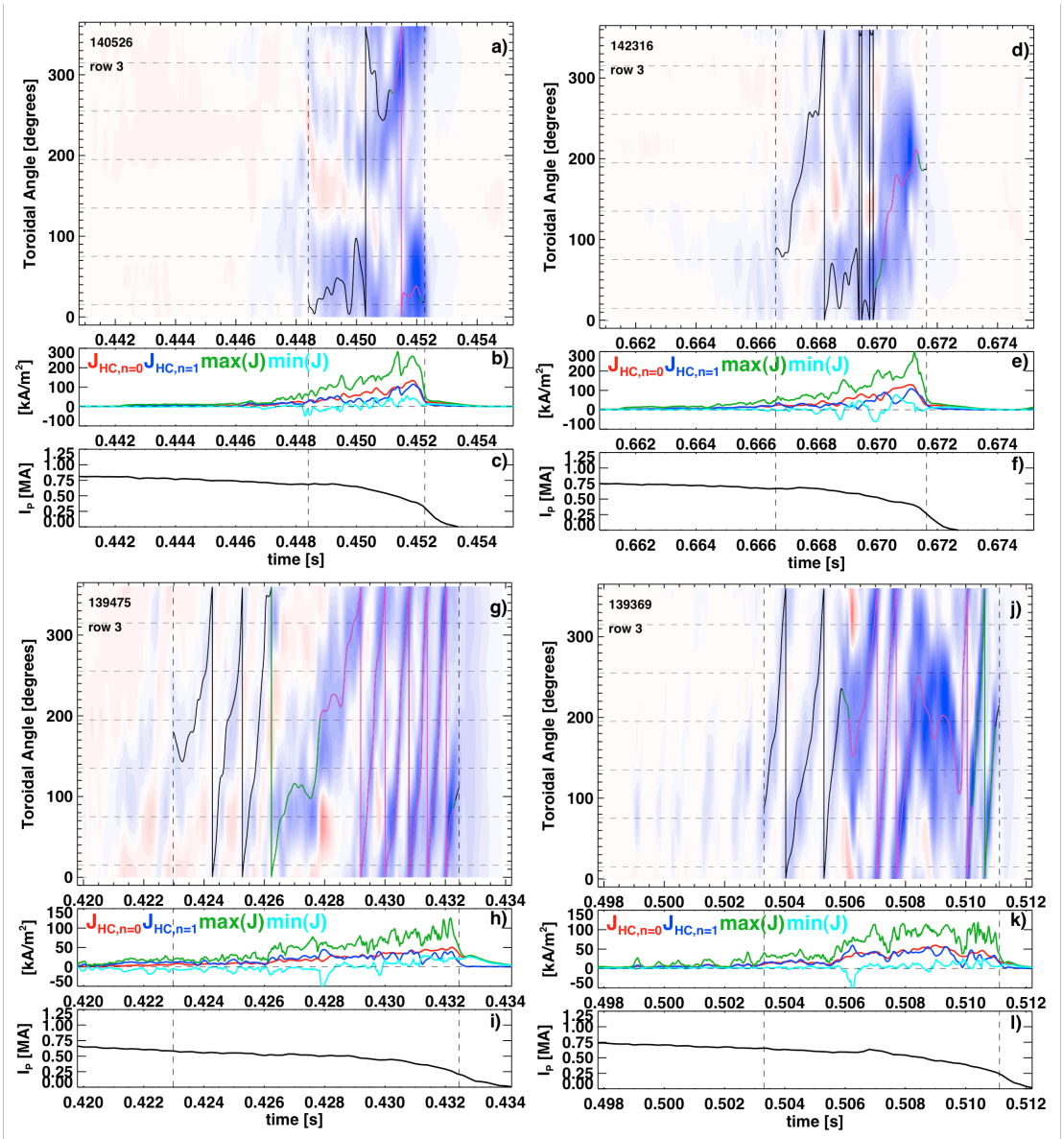

Fig. 6: Four additional examples of the halo current asymmetry evolution. The time window is 14 ms long for each case. See text for further details.

Fig. 6g) through 6i) shows an example where, as in Fig. 2, there is substantial rotation of the halo current pattern observed. In this case, the initial low-level currents starting at t~0.423 are already rotating. The rotation appears to stagnate twice, at t=0.427 and t=0.4285, before beginning a phase of rapid rotation. In this case, 7 total revolutions of the halo current pattern are observed.

Fig. 6j) through 6l) shows an example where the halo current rotation behaves in an apparently erratic manner. A low level of current begins to flow at t=0.503, and unlike the case in Fig. 2 but like that in Fig. 6g), has clear toroidal rotation. There is a period of stagnation at t=0.506, but the rotation is then resumed. However, at t=0.508 s, the

rotation actually changes sign, rotating slowly in the co-I_P direction. This lasts until t=0.51, after which the pattern makes two rapid rotations in the counter-I_P direction.

In all cases, the n=0 and n=1 halo current magnitudes are comparable through the duration of the pulse. The minimum halo current measured on any tile typically hovers around zero, except for small transients. Finally, all of the examples in Fig. 6 show a late symmeterization of the halo current pulse. This is most clear in the example in Figs. 6g) and h), but can be found to a lesser extent in all other cases.

The dynamics of the "erratic" discharge, 139369 in Fig. 6j)-6l), are illustrated in greater detail in Fig. 7; the analysis techniques here are the same as described relation to Fig. 4. The baseline (f_0) and toroidally localized (f_1) components of the current are shown in Fig 7a), along with the minimum and maximum currents. It is clear again that the purely axisymmetric part is rather small in magnitude during most of the halo current pulse. The maximum instantaneous current is again comparable to the value of f_1.

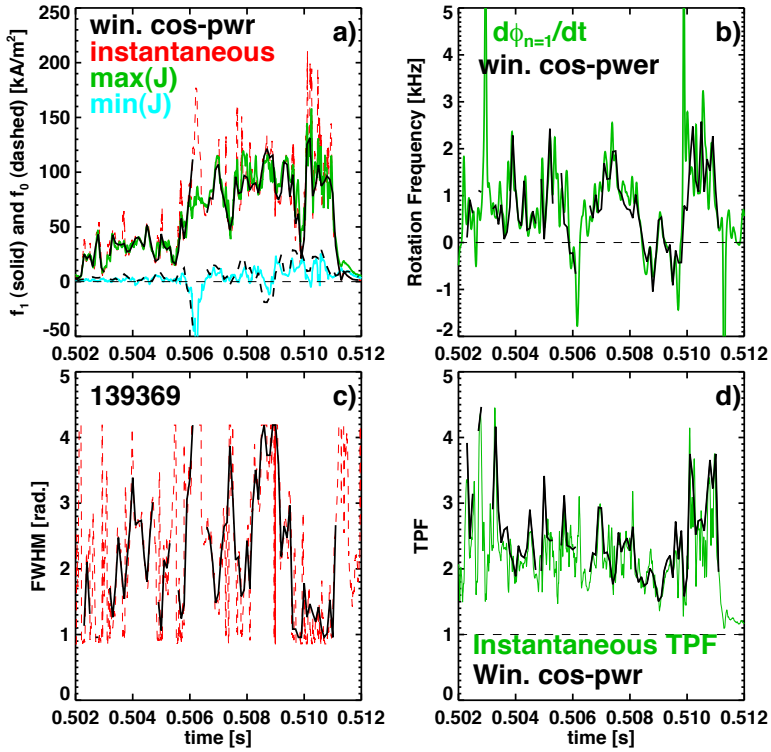

Fig. 7: Details of the toroidal asymmetry dynamics for the discharge in Fig. 6j) through 6l), which shows rather erratic behavior of the halo current rotation. The quantities plotted are the same as in Fig. 4.

The rotation velocities are shown in Fig. 7b), where both the fits during time windows (black) and the differentiation of the n=1 phase (blue) are shown. This figure illustrates a phase between 0.502 and 0.5058 s during which the rotation is fairly uniform. There is then a short phase of rotation in the co-I_P direction, at t=0.506. The rotation then returns to the counter-I_P direction for ~2 ms, with rotation frequencies of ~1 kHz. This is followed by a second stagnation and reversal of the rotation between t=0.508 and 0.510. Finally, a burst of rotation at t=0.510 results in the final two toroidal revolutions.

The full-width at half maximum in Fig. 7c) and the peaking factor in Fig. 7d) also show quite complicated temporal dynamics. The FWHM shows periods where the lobe is quite narrow (FWHM ~ <2 radians), and cases where it is quite broad; interestingly, the periods with a broad lobe at t=0.506 and t=0.509 correspond to the two stagnations in the rotation velocity. The TPF also varies rapidly, with a mean of ~2 through most of the halo current pulse.

To summarize this session, the examination of individual discharges demonstrates that the dynamics of halo currents can be quite complicated. Essentially all cases have a significant toroidal asymmetry; indeed, the dominant structure is typically a large lobe of current, whose toroidal localization may be significantly more severe than a simple n=1 cosine dependence. This asymmetry is often observed to rotate toroidally, though the frequency can vary substantially during the relatively short period with large halo currents. The characteristic width of the asymmetry and associated peaking factor can also vary rapidly during a single discharge.

4: Statistical analysis halo current dynamics

In order to establish the relative occurrence levels for these various events, a database of the 732 discharges with the largest halo currents observed by the row-3 tiles has been formed. The typical rotation speed, number of rotations, and pulse durations were established, averaged over the periods when the n=1 halo current is greater than 25%, 50%, and 75% of its maximum in that pulse (the 25%, 50%, and 75% basis in the plot captions). Note here that because the shape of the n=0, n=1, and max(J) (or min(J)) curves are so similar on Figs. 2, 5, & 6, the time windows would not be meaningfully different if a criterion other than the n=1 amplitude were used in the determining the averaging windows. Also included in the database are the various equilibrium properties of the plasma before the disruption and information about any magnetic braking applied to the plasma.

A set of results from these studies in shown in Fig. 8, where the colors indicate the averaging window as per Fig. 3. A histogram of rotation frequencies is shown in Fig. 8a). For any of the 25%, 50%, or 75% basis, the most typical rotation frequencies are <~700 Hz in NSTX. However, for the higher percentage basis calculations, which are localized to a smaller time during the halo current pulse, rotation frequencies of up to 2 kHz have been observed.

The durations of the various periods are shown in Fig. 8b). For the 75% basis, corresponding to the period of peak halo current, the durations are most commonly 0.5-2.5 ms, but with a tail out to ~ 6 ms. For the 25% basis, encompassing the majority of the halo current pulse, the durations are typically ~3 to ~6 ms long.

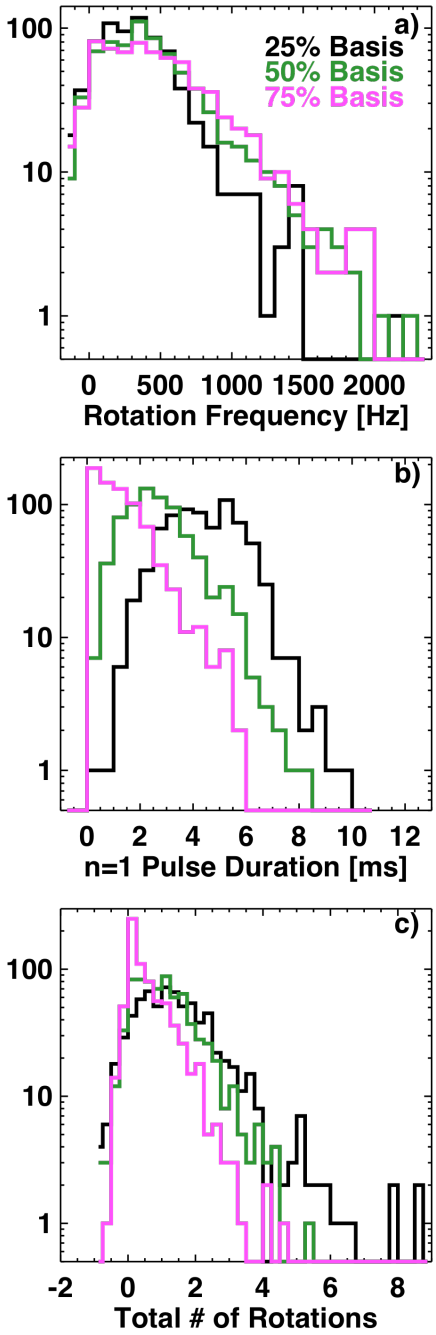

Fig. 8: Histograms of the a) the rotation frequency, b) the halo current duration, and c) the total number of revolutions, for a database of 732 discharges. The color code corresponds to different phases of the halo current pulse, as described in Fig. 3, and all cases are downward VDEs roughly similar to that in Fig. 2. Note the logarithmic scale on the y-axis.

Figure 8c) shows the total number of rotations. For the 25% basis, there are examples with up to 8 toroidal revolutions. For the 50% basis, that number is reduced to 5, while it drops to ~4 for the 75% basis. Note that the numbers in these figures are consistent, in that, taking the 25% basis as an example, typical durations of 5 ms and

rotation frequencies of 300 Hz imply that ~1.5 revolutions should be common, as is found in Fig. 8c).

A key question is whether these rotation dynamics are strongest in cases with larger or smaller halo currents. This is answered in Fig. 9, where the rotation frequency, pulse duration, and total number of revolutions are plotted as a function of two measures of the halo current magnitude. The first measure is the simple n=0 current magnitude, calculated as the average of the current in the six tiles at each time step. The second metric is the instantaneous maximum of the six halo current signals, motivated by the discussions in Sect. 3. In both cases, the plotted current is averaged over the time when the n=1 magnitude is greater than 50% of the peak.

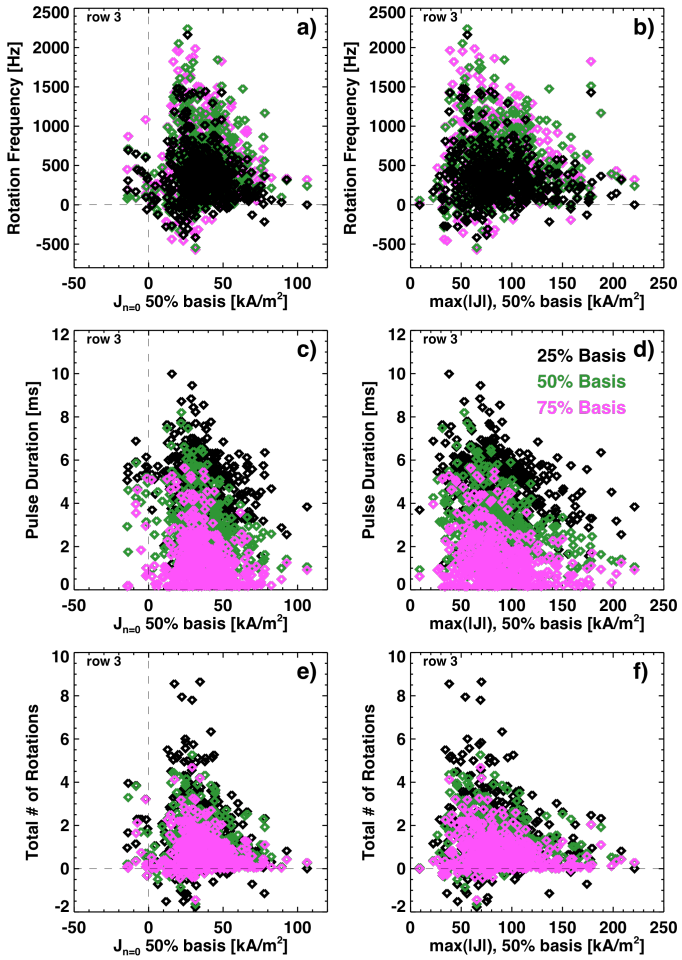

Fig. 9: Plots of the rotation frequency in a) and b), pulse duration in c) and d), and total number of revolutions in e) and f). The left column shows that data plotted against the n=0 halo current magnitude averaged over the 50% time-window, while the right column shows the data plotted against the maximum measured current density, averaged over the 50% time-window

Fig. 9a) and 9b) show the rotation frequency of the asymmetry, determined on the 25%, 50% and 75% basis, as a function of the n=0 and maximum halo current. In both cases, there is a strong trend for the rotation frequency to be rather small when the halo

current amplitudes are strongest, and for the largest halo current rotation frequencies to occur in cases with cases with smaller halo currents. The pulse durations are shown in Fig. 9c) and 9d). Once again, there is a clear trend of longer pulse durations when the halo current magnitude is smaller, and shorter durations when the magnitude is larger.

The net result of these trends is shown in Fig. 9e) and 9f). The total number of rotations tends to be a strong function of the total halo current magnitude. Cases with large halo currents tend to have a small number of rotations, while those with smaller halo currents often, but not always, have larger numbers of rotations. This statement is true whether the halo current magnitude is measured by the toroidally average component or by the maximum local halo current.

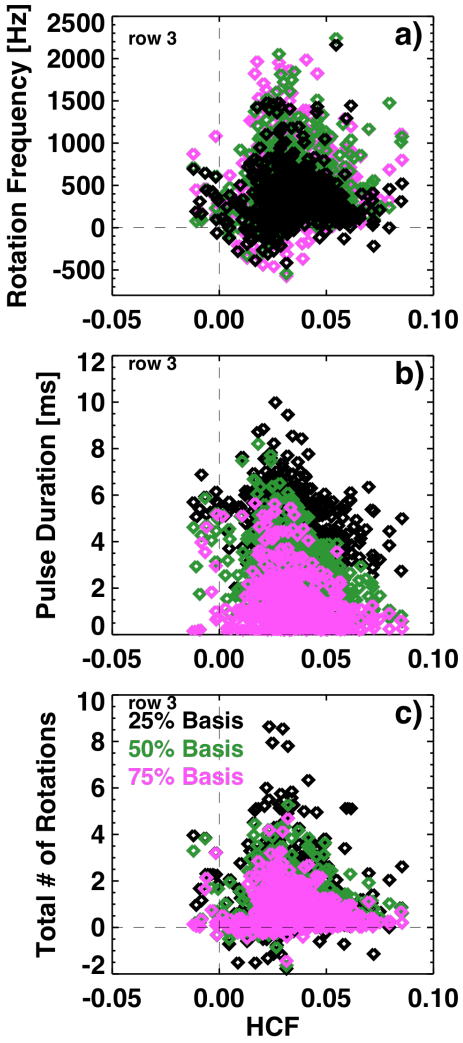

Fig. 10: Plots of the rotation frequency in a), pulse duration in b), and total number of revolutions in c), as a function of the halo current fraction, averaged over the period when the n=1 halo current is greater than 50% of its maximum value. See text for additional details.

The absolute magnitude of the halo currents, measured in amperes, will of course vary from device to device. The most common normalization of the halo current

magnitude is the plasma current itself, here denoted $I_{P,D}$ and measured just before the initiation of the final current quench [5,6]; this is called the halo current fraction (HCF). Here, the total halo current is estimated by taking the average current measured by the six tiles at each time and multiplying it by the ratio of the area of all tiles in row 3 of the outboard divertor to the area of the six measuring tiles. The halo current fraction so defined is then averaged over the period where the n=1 halo current is greater than 50% of its maximum value.

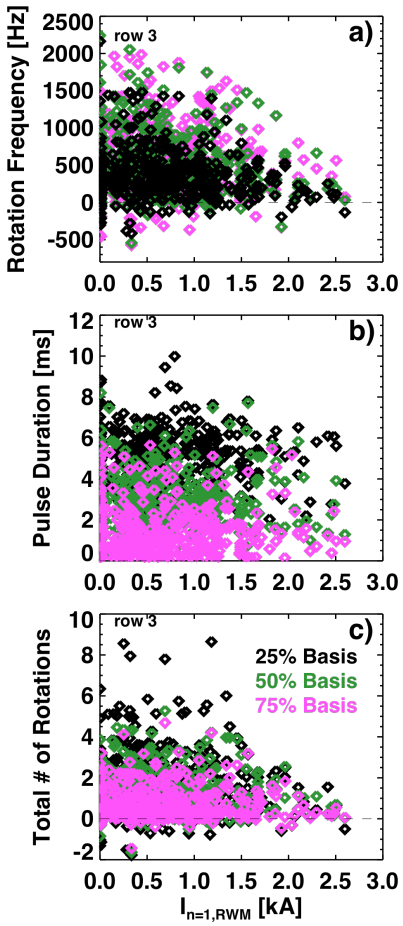

Fig. 11: Plots of the rotation frequency in a), pulse duration in b), and total number of revolutions in c), as a function of the n=1 applied field.

The results of such analysis are shown in Fig. 10. Frame a) shows a general trend of the rotation frequency decreasing with halo current fraction, though there are some clear outliers at large halo current fraction and large rotation frequency. Fig 10b) shows that the pulse durations tend to drop rapidly as the halo current fraction increases. This emphasizes that cases with large halo currents tend to have them for only a short amount of time. The result of these two observations is that the total number of rotations tends to decrease rapidly as the halo current fraction is increased. This is a positive result for future tokamak/ST facilities, as it implies that the largest resonant amplification factors may not be applied to the largest halo loads. However, confirmation of this trend on other devices is clearly required before it can be extrapolated to ITER.

5: Effect of n=1 fields on halo current rotation

The impact of large n=1 field on the rotation dynamics has also been studies. This has been done in by i) examining a large database of NSTX discharges, and ii) applying n=1 fields to deliberate VDEs. Those two studies will be discussed in that order in this section. These studies are motivated by the observation that n=1 fields can brake the plasma rotation, by applying either a localized JxB torque at the integer q surfaces [53], or a more radially distributed torque from neoclassical toroidal viscosity (NTV) [54-56]

NSTX has an array of six midplane radial field coils [57], which are used for magnetic braking [56,58,59], dynamic n=1 error field correction [60], pre-programmed n=3 error field correction [61], and fast n=1 RWM control [59,62]. It is common for the final-mentioned use of the system to apply large n=1 fields during the disruption, both due to the actual 3D distortions of the plasma and inaccuracies in reconstructing the magnetic perturbation amplitudes during rapid disruption dynamics. As a consequence, many different levels of applied n=1 fields were present during the disruptions studied in this paper.

Fig. 11a) shows the typical rotation frequencies as a function of the n=1 applied field amplitude, as measured by the coil currents; the maximum allowed power supply current is 3.2 kA. It is immediately clear that the rotation frequency, measured on any of the 25%, 50%, or 75% basis, is reduced for large values of the n=1 applied field. The pulse duration in Fig. 11b), however, is largely independent of the applied field magnitude. The net result, shown in Fig. 1c, is that total number of revolutions is reduced when the n=1 applied field magnitude is large.

Of course, the coil current magnitudes are an NSTX-specific quantity. To put them in perspective, the n=1 B_R perturbation at the midplane has been computed, on a circle with radius R=1.45 m (approximately the outboard midplane radius for H-mode plasmas). Note that this calculation does not include poloidal mode number information. The resulting field amplitudes are ~0.012 G/A of n=1 B_R perturbation. This implies that the 2.5 kA n=1 perturbations in Fig. 11 correspond to ~30 G of n=1 applied field. When the same analysis is computed for a circle displaced to Z=-1 m, but still at R=1.45, the resulting n=1 B_R perturbation is ~0.0015 G/ kA, corresponding to ~4 G of n=1 perturbation. These should be compared to the 4.5 kG (at R~1 m) toroidal fields that are most common in NSTX experiments; the applied field magnitudes that appear to result in some suppression of the halo current asymmetry rotation are between $6x10^{-3}$ and 10^{-4} of the applied toroidal field.

In the specific experiments, large n=1 fields were applied during deliberate VDEs. These were quite rapid VDEs, where radial field feedback was deliberately frozen [63] at t= 0.3 s; the plasma was then actively pushed down by applying a positive bias to the upper radial field coil and a negative bias to the lower radial field coil. The vertical motion under these scenarios begins to clearly grow at ~310 ms, with, as shown in Fig 12a), disruption following at ~340 ms. These scenarios produce the largest halo current

fractions measured in NSTX [41]. As shown in Fig. 12b), n=1 fields with current amplitudes of 750, 1000, and 1500 A were applied, starting at 0.3 seconds. This is sufficiently late that the fields do not impact the main portion of the discharge, but sufficiently early that the fields can penetrate the vessel and passive plates by the time of large halo currents.

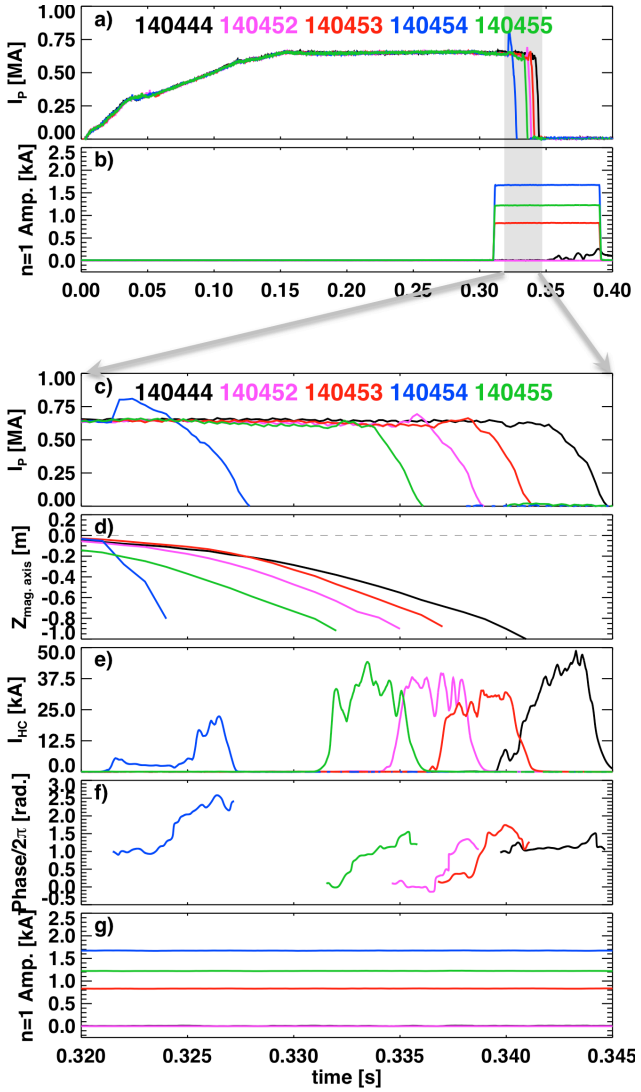

Fig. 12: Plots of a) the plasma current and b) the applied n=1 field in the upper figure. for VDE disruptions. The lower figure shows c) the plasma current, d) the magnetic axis location, e) the n=0 halo current magnitude, f) the n=1 asymmetry phase, and g) the n=1 applied field magnitude, during a small time-window containing the disruption.

The results of this experiment are shown in Fig. 12c) through 12g). Discharges 140444 and 140452 are reference discharges with no n=1 applied fields. They have quite similar VDE growth rates and disruption times. One of them (140452) shows approximately 1 revolution worth of rotation; the other (140444) shows essentially no

toriodal rotation. Note that because these deliberate VDEs tend to have very large halo currents and halo current fractions [41], the data in Fig. 10 indicates that many toroidal revolutions should not be expected under those conditions.

Discharges 140453, 140454, and 140455 have 750, 1500 kA, and 1000 kA of n=1 current respectively. All three of these cases show ~1.5 total revolutions, which is comparable to that in one of the reference cases, and exceeds the number of revolutions in the other. Note that the case with 1500 kA of n=1 coil current actually disrupts before contact with the divertor floor is made; it appears likely that an n=1 locked mode is driven in this cases. Nevertheless, tordoidal rotation of the asymmetry is observed.

The conclusions of this section are thus somewhat mixed. There is some evidence that very large n=1 fields can eliminate the cases with many toroidal rotations. However, in VDE disruptions prone to having large halo currents and only a single toroidal revolution, the n=1 applied fields had no apparent impact on the rotation dynamics.

6: Halo current symmeterization during the late current quench.

As noted in the context of Figs 2-6, there is a tendency for the halo current entrance point magnitude to become tordoidally symmetric during the last phase of the disruption. This section will show a likely explanation for this observation: that the symmeterization time corresponds to the time when the magnetic axis has been nearly or completely driven into the lower divertor plate, and the open field line currents dominate.

There does not exist a code that can compute the experimentally-constrained 3D or 2D force-balance equilibria during this phase of the discharge. In particular, the 2D equilibrium fitting codes used at NSTX, EFIT first described in Ref. [64] and implemented at NSTX as per Refs. [66,65], and LRDFIT [67], have typically not been run in a way allowing current outside the separatrix. Rather, the toroidal currents are related to the pressure and current profiles as per the Grad–Shafranov equation, $J_\phi = Rp' + \frac{\mu_0}{R} ff'$, where the pressure p and f=RB_T are functions of poloidal flux within the separatrix [68].

Instead, the disrupting plasma is modeled as a group of axisymmetric filaments. This fitting procedure, part of the LRDFIT code, uses a regularization scheme in order to prevent unphysical current variation; it also includes axisymmetric equivalent currents in the vacuum chamber wall. Note that the solutions so computed do not have an MHD force balance constraint, and so should be viewed as approximations to the true evolution.

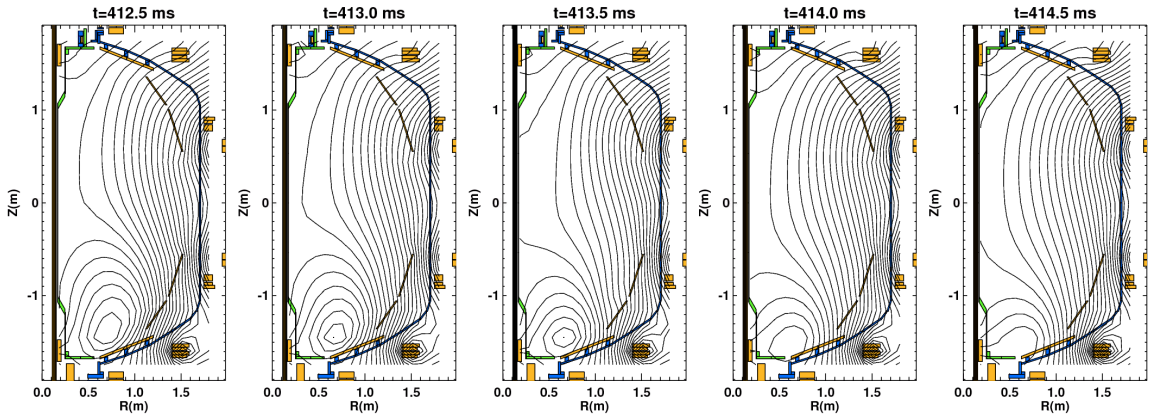

Fig. 13: Evolution of the poloidal magnetic flux during the later phase of a VDE, as determined by a filament reconstruction code. The discharge in this case (141687) is the same as in Fig. 2.

With that caveat, Fig. 13 illustrates five time-slices during the later phases of the disruption, for the discharge already discussed in Figs. 2 and 4. The boundaries plotted in Fig. 2b) indicate that this discharge ultimately limits on the lower-outer divertor, and this is observed in the filament reconstruction at t=412.5 ms. The plasma continues to move down, with the magnetic axis lost at t~414 ms. The last reconstruction shows that some residual current is present, but that the magnetic surface configuration has essentially vanished. Looking back at Fig. 2, the halo current asymmetry has essentially vanished at t=413.6. It can thus be inferred that the near or complete loss of the closed magnetic surface geometry during the VDE results in the loss of the halo asymmetry.

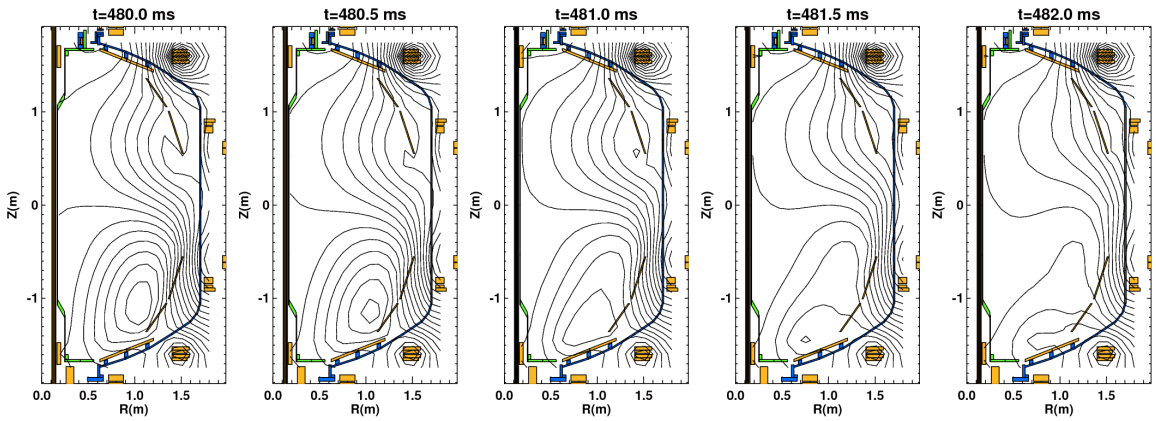

Fig. 14: Evolution of the poloidal magnetic flux during the later phase of a VDE, as determined by a filament reconstruction code. The discharge in this case (141687) is the same as in Fig. 5.

A similar calculation has been done for the discharge in Fig. 5; note that the discharge in that figure limited on the lower secondary passive plates, and that a similar phase of nearly axisymmetric halo current was observed at the end of the disruptions. The SVD poloidal flux reconstruction is shown in Fig. 14, and shows closed poloidal flux contours limiting on the lower passive plate. This closed-flux configuration is essentially eliminated by t=481 ms, which approximately corresponds to the time in Fig. 5 where the halo currents become toroidally symmetric.

7: Summary and Discussion

This paper has documented a number of features of the halo current asymmetry in NSTX. These include:

- The halo current toroidal asymmetry is often observed to rotation toroidally, with up to 8 total rotations detected in extreme cases (Sections 3 & 4).
- In many cases, the dominant pattern of the halo current is a toroidally localized lobe, with full width at half maximums of 1.5-4 radians (Section 3).
- The temporal dynamics of this rotation can be quite complicated, with rapid variations in both the rotation velocity and toroidal peaking (Section 3).
- The cases with the largest halo currents typically have both smaller rotation speeds and fewer rotations (Section 4).
- It appears that very large n=1 applied fields may be able to eliminate the cases with many toroidal rotation. However, large n=1 fields were not observed to change the rotation dynamics in scenarios with ~1 toroidal revolution (Section 5).
- The halo current asymmetry typically vanishes during the very final phase of the disruption, approximately 1 ms before the n=0 halo current vanishes. This is likely due to the near or complete loss of closed-surface magnetic geometry at the end of this phase, with residual open-field line current dominating the system (section 6).

A few comments are in order to place these results in the context of the previous overview of NSTX halo currents, in Ref. [41]. Fig. 7d) of that paper shows a plot of the toroidal peaking factor as a function of the halo current fraction for the row-3 tiles, measured at the time of maximum halo current fraction. There is considerable scatter in that plot. In part this can be understood by looking at the TPF evolution in Figs. 4d) and 7d) of the present paper. There, it is clear that small changes in the time at which the TPF is evaluated can result in large changes in the TPF so determined. Additionally, note that the row 3 halo current fractions in that previous paper are larger than in Fig. 10 of the present paper, due to the fact that the present paper uses averages over different phases of the pulse, while the previous paper took the maximum halo current magnitude.

The previous paper also noted that the toroidal peaking in the chamber wall appears to be less peaked than at the entrance points. The likely explanation for this is that the currents tend to become more toroidally uniform in the large conducting structures such as the NSTX vacuum chamber. This reduction of the halo current peaking in the vacuum chamber, in particular, the center column of a spherical torus, has been observed computationally in Refs [69] and [70].

Some of these results are potentially optimistic for future tokamak/ST reactor facilities. For instance, the observation that the largest halo currents (or halo current fractions) typically do not have many revolutions of the asymmetry is generally beneficial. The trend toward symmeterization later in the halo current phase reduces to some extent the duration of strong asymmetry. However, without a more complete

understanding of the underlying rotation physics or confirmation of these trends on other, larger devices, it is difficult to extrapolate the results to future tokamaks and STs.

Acknowledgements
The author would like to thank Allen Boozer for encouragement and helpful discussion. This research was funded by the United States Department of Energy under contract DE-AC02-09CH11466.

References

[1] "ITER Physics Basis", Nuclear Fusion **39**, 2137 (1999).
[2] T.C. Hender, et al., Nuclear Fusion **47**, S128 (2007).
[3] D.A. Humphreys and D.G. Whyte, Phys. Plasmas **7**, 4057 (2000).
[4] V. Riccardo, P. Barabaschi, and M. Sugihara, Plasma Phys. Control. Fusion **47**, 117 (2005).
[5] J.C. Wesley, et al., *Disruption Characterization and Database Activities for ITER*, paper IT/P1-21, IAEA FEC, Chengdu China (2006)
[6] S.P. Gerhardt, J. E. Menard, and the NSTX Team, Nuclear Fusion **49**, 025005 (2009).
[7] J.C. Wesley, et al., *Disruption, Halo Current and Rapid Shutdown Database Activities for ITER,* paper ITR/P1-26, IAEA FEC, Deajeon, Korea (2010).
[8] Y. Shibata , et al., Nuclear Fusion **50**, 025012 (2010).
[9] V. Riccardo, et al., Plasma Phys. Control Fusion **44**, 905 (2002).
[10] V. Riccardo, A. Loarte, and the JET EFDE Contributors, Nuclear Fusion **45**, 1427 (2005).
[11] M. Sugihara, et al., Nuclear Fusion **47**, 337 (2007).
[12] G. Arnoux, A. Loarte, V. Riccardo, W. Fundamenski, A. Huber and JET-EFDA contributors, Nuclear Fusion **49**, 085038 (2008).
[13] V Riccardo, et al., Plasma Phys. Control. Fusion **52**, 024018 (2010).
[14] M.N. Rosenbluth and S.V. Putvinski, Nuclear Fusion **37**, 1355 (1997).
[15] R. Yoshino, S. Tokuda and Y. Kawano, Nuclear Fusion **39**, 151 (1999).
[16] R. Yoshino, and S. Tokuda, Nuclear Fusion **40**, 1293 (2000).
[17] R.D. Gill, et al., Nuclear Fusion **42**, 1039 (2002).
[18] H. Tamai, et al., Nuclear Fusion **42**, 290 (2002).
[19] V.V. Plyusnin, et al., Nuclear Fusion **46**, 277 (2006)
[20] M. Forster , et al., Nuclear Fusion **51**, 043003 (2011).
[21] E.M. Hollmann, et al., Nuclear Fusion **51**, 103026 (2011).
[22] N.W. Eidietis, et al, Phys. Plasmas **19**, 016109 (2012).
[23]A.N. James, et al, Nuclear Fusion **51**, 103026 (2011).
[24] V. Sizyuk and A. Hassanein, Nuclear Fusion **49**, 095003 (2009).
[25] M.J. Schaffer and B.J. Leikund, Nuclear Fusion **31**, 1750 (1991).
[26] E. J. Strait, et al., Nuclear Fusion **31**, 527 (1991).
[27] D.A. Humphreys and A.G. Kellman, Phys. Plasmas **6**, 2742 (1999).
[28] N.W. Eidietis and D.A. Humphreys, Nuclear Fusion **51**, 083034 (2011).
[29] Andrew, P. Noll, P. Riccardo, V. Proc. 17th IEEE/NPSS Symposium on Fusion Engineering (1997) 108.
[30] V. Riccardo, et al., Fusion Engineering and Design, **66-68**, 919 (2003).
[31] V. Riccardo and JET EFDA contributors, Plasma Phys. Control. Fusion **45**, A269 (2003).
[32] V. Riccardo, et al., Plasma Phys. Control. Fusion **46**, 925 (2004).
[33] V. Riccardo, et al., Nuclear Fusion **49**, 055012 (2009).
[34] T C Hender, et al., *JET Disruption Studies in Support of ITER*, paper EXS/10-3, IAEA FEC 2010, Daejon, Korea, http://www-pub.iaea.org/mtcd/meetings/PDFplus/2010/cn180/cn180_papers/exs_10-3.pdf
[35] G. Pautasso and O. Gruber, Fus. Sci. and Tech. **44**, 716 (2003)
[36] G. Pautasso, et al., Nuclear Fusion **51**, 1 (2011).

[37] P.J. Knight, et al., Nuclear Fusion **40**, 325 (2000).
[38] Y. Neyatani, et al, Nuclear Fusion **39**, 559 (1999).
[39] R. S. Granetz, et al., Nuclear Fusion **36**, 545 (1996).
[40] G. F. Counsell, R. Martin, T. Pinfold, D. Taylor, and the MAST team, Plasma Phys. Control. Fusion **49**, 435 (2007).
[41] S.P. Gerhardt, et al., Nuclear Fusion **52**, 063005 (2012).
[42] L. E. Zakharov, Phys. Plasmas **15**, 062507 (2008).
[43] L. E. Zakharov, Phys. Plasmas **18**, 062503 (201).
[44] A. H. Boozer, Phys. Plasmas **19**, 058101 (2012).
[45] A. H. Boozer, Phys. Plasmas **19**, 052508 (2012)
[46] J. Manickam, A. Boozer, and S. Gerhardt, Phys. Plasmas **19**, 082103 (2012).
[47] M. Ono, et al., Nuclear Fusion **40**, 557 (2000).
[48] T. Stevenson, et al., *A neutral beam injector upgrade for NSTX*, PPPL Report 3651 (2002).
[49] J.R. Wilson, et al., Phys. Plasmas **10**, 1733 (2003).
[50] S.P. Gerhardt, et al., Rev. Sci. Instrum. **82**, 103502 (2011).
[51] H.W. Kugel, et al., Fusion Engineering and Design **84**, 1125 (2009).
[52] Markwardt, C. B. 2008, "Non-Linear Least Squares Fitting in IDL with MPFIT," in proc. *Astronomical Data Analysis Software and Systems XVIII*, Quebec, Canada, ASP Conference Series, Vol. 411, eds. D. Bohlender, P. Dowler & D. Durand (Astronomical Society of the Pacific: San Francisco), p. 251-254 (ISBN: 978-1-58381-702-5
[53] R. Fitzpatrick, Nuclear Fusion **33**, 1049 (1993).
[54] K.C. Shaing, Phys. Fluids **26**, 3315 (1983).
[55] K.C. Shaing, Phys. Plasmas **10**, 1443 (2003).
[56] J.-K. Park, et al, Phys. Rev. Lett **102**, 065002 (2009).
[57] A. Sontag, et al. Nuclear Fusion **47**, 1005 (2007).
[58] W. Zhu, et al., Phys. Rev. Lett **96**, 225002 (2006).
[59] S.A. Sabbagh, et al., Nuclear Fusion **50**, 025020 (2010)
[60] J.E. Menard, et al., Nuclear Fusion **50**, 045008 (2010)
[61] S. P. Gerhardt, et al., Plasma Phys. Control. Fusion **52**, 104003 (2010).
[62] S.A. Sabbagh, et al., Phys. Rev. Lett. **97**, 045004 (2006).
[63] D.A. Humphreys, et al, Nuclear Fusion **49**, 115003 (2009).
[64] L. L. Lao, et al., Nuclear Fusion **25**, 1421 (1985).
[65] S.A. Sabbagh, et al, Nuclear Fusion **41**, 1601 (2001).
[66] S.A. Sabbagh, et al, Nuclear Fusion **46**, 635 (2006).
[67] J. E. Menard, et al., Phys. Rev. Lett **97**, 095002 (2006)
[68] J. Wesson, *Tokamaks*, Clarendon Press, Oxford, England, 1997
[69] N. Pomphrey, J.M. Bialek, and W. Park, Nuclear Fusion **38**, 449 (1998).
[70] J.E. Menard, et al., Nuclear Fusion **52**, 083015 (2012)

The Princeton Plasma Physics Laboratory is operated
by Princeton University under contract
with the U.S. Department of Energy.

Information Services
Princeton Plasma Physics Laboratory
P.O. Box 451
Princeton, NJ 08543

Phone: 609-243-2245
Fax: 609-243-2751
e-mail: pppl_info@pppl.gov
Internet Address: http://www.pppl.gov